Title
Phase stability of iron germanate, FeGeO3, to 127 GPa

Authors
Dutta, R
Tracy, SJ
Stan, CV
et al.

Peer reviewed

1   **Phase Stability of Iron Germanate, FeGeO$_3$, to 127 GPa**

2   R. Dutta[1], S. J. Tracy[1], C. V. Stan[2, 3], V. B. Prakapenka[4], R. J. Cava[2] and T. S. Duffy[1]

3   [1]Department of Geosciences, Princeton University, NJ 08544, USA.

4   [2]Department of Chemistry, Princeton University, NJ 08540, USA.

5 [3]Now at: Advanced Light Source, Lawrence Berkeley National Laboratory, Berkeley, CA 94720,

6   USA.

7 [4]GeoSoilEnviroCARS, University of Chicago, Argonne National Laboratory, Argonne, IL 60439,

8   USA.

9

10**Abstract**

11   The high-pressure behavior of germanates is of interest as these compounds serve as

12analogs for silicates of the deep Earth. Current theoretical and experimental studies of iron

13germanate, FeGeO$_3$, are limited. Here, we have examined the behavior of FeGeO$_3$ to 127 GPa

14using the laser-heated diamond anvil cell combined with *in situ* synchrotron X-ray diffraction.

15Upon compression at room temperature we find that the ambient-pressure clinopyroxene phase

16transforms to a disordered triclinic phase (FeGeO$_3$ (II)) at ~ 18 GPa in agreement with earlier

17studies. An additional phase transition to FeGeO3 (III) occurs above 54 GPa at room

18temperature. Laser-heating experiments (~1200-2200 K) were conducted at three pressures (33,

1954 and 123 GPa) chosen to cover the stability regions of different GeO$_2$ polymorphs. In all cases,

20we observe that FeGeO$_3$ dissociates into GeO$_2$ + FeO at high-pressure and temperature

21conditions. Neither the perovskite nor the post-perovskite phase was observed up to 127 GPa at

22ambient or high temperatures. The results are consistent with the behavior of FeSiO$_3$, which also

23dissociates into a mixture of the oxides (FeO + SiO$_2$) at least up to 149 GPa.
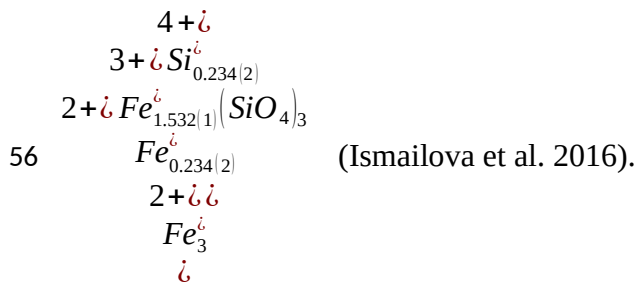
24**Introduction**

25   Bridgmanite, ((Mg,Fe)SiO$_3$, Pv), belongs to the family of ABO$_3$ oxide perovskites and

26crystallizes in the orthorhombic system (Space group: *Pbnm*). The structure consists of a three-

27dimensional network of corner-linked BO$_6$ octahedra surrounding distorted 8-coordinated A sites.

28Bridgmanite is of geophysical interest as it is expected to be the most abundant phase in the

29Earth's lower mantle below 660-km depth. Under pressure and temperature conditions

30approaching those of the core-mantle boundary of the Earth (~125 GPa, >2000 K), Mg-rich

31bridgmanite undergoes a phase transition to the $CaIrO_3$-type structure known as post-perovskite

32(pPv) (Murakami et al. 2004; Oganov and Ono 2004). The post-perovskite phase also crystalizes

33in the orthorhombic crystal system (Space group: *Cmcm*) and has the same coordination numbers

34as perovskite. In contrast to the corner-sharing octahedral network in the perovskite structure, the

35silicate octahedra share edges and corners in pPv giving rise to a structure layered along the *b*

36crystallographic axis.

37   The role of iron in deep Earth silicates is of key importance due to seismic evidence for

38possible Fe-enriched regions of the deep Earth (Lay et al. 2006). In addition, high-pressure spin

39transitions in Fe-bearing minerals have attracted much attention (Lin et al. 2013; Badro 2014).

40For the iron end-member of the $(Mg,Fe)SiO_3$ system, the stability of different high-pressure

41phases has been explored by theoretical studies at high pressures. The post-perovskite phase of

42$FeSiO_3$ is reported to be more stable than the perovskite phase above 35 GPa on the basis of

43density functional theory (DFT) calculations at 0 K (Stackhouse et al. 2006). Using an

44evolutionary algorithm together with DFT, Cohen and Lin (2014) proposed a possible high-

45pressure (100 GPa) structure of $FeSiO_3$ called PPv-II (*Cmmm*). PPv-II was predicted to be less

46stable than both Pv and pPv at T = 0 K, but could be entropically stabilized at high temperatures.

47   Experimentally, iron-rich perovskites and post-perovskites in the $(Mg,Fe)SiO_3$ system

48have been synthesized with Fe# (Fe# = $Fe/¿\frac{Mg+Fe}{}$)) up to 0.75 (Tateno et al. 2007; Dorfman et

49al. 2013) and 0.8 (Mao et al. 2004). However, end-member $FeSiO_3$ has been shown to dissociate

50into the respective oxides (SiO_2 + FeO) in experiments up to 25 GPa (Ming and Bassett 1975)

51and 149 GPa (Fujino et al. 2009). It has also been suggested that (Mg Fe)SiO$_3$ perovskite

52dissociates at high P-T (95 – 101 GPa, 2200 – 2400 K) to a Fe-poor perovskite and a hexagonal

53Fe-rich phase called "H phase" (Zhang et al. 2014).. A perovskite of almandine composition

54(Fe$_3$Al$_2$Si$_3$O$_{12}$ or (Fe,Al)(Si, Al)O$_3$) is stabilized above 80 GPa (Dorfman et al. 2012). Finally, a

55recent study reported synthesis of pure Fe-bridgmanite in the ferric iron system with composition

56
$$Fe^{2+}_{0.234(2)}\left[Fe^{3+}_{1.532(1)}\begin{pmatrix}Si^{4+}_{0.234(2)}\\Fe^{2+}\end{pmatrix}\right]\left(SiO_4\right)_3$$
(Ismailova et al. 2016).

57   Germanates are known to be effective analogs for silicates as they undergo similar

58sequences of phase transitions but at lower pressures (Ringwood and Seabrook 1963; Stan et al.

592017). For example, the Pv-pPv transition occurs near 65 GPa in MgGeO$_3$ (Hirose et al. 2005)

60compared to ~125 GPa in the corresponding silicate. In the (Mg,Fe)GeO$_3$ system, iron-bearing

61Pv and pPv have been synthesized at high-pressure with Fe# ≤ 52 (Stan et al. 2017). Here, we

62explore the analog end-member composition FeGeO$_3$ to understand its high-pressure behavior.

63   At ambient conditions, iron germanate crystallizes in the *C2/c* clinopyroxene structure

64(Royen and Forwerg 1963) Previous high-pressure work on FeGeO$_3$ is limited and somewhat

65unclear. Under room-temperature compression, a reversible phase transition to a triclinic phase (

66 $P\bar{1}$ designated as FeGeO$_3$(II) was observed between 13 and 20.1 GPa (Hattori et al. 2001).

67 Evidence for transformation of FeGeO$_3$ to the perovskite structure at room temperature has been

68 reported above 33 GPa (Nagai et al. 1998; Hattori et al. 1999). However, this result may be

69 considered inconclusive as the reported X-ray diffraction peaks are weak and broad. Upon

70 decompression to ambient conditions, the sample was found to adopt the LiNbO$_3$-type structure

71 (Hattori et al. 1999), as does MgGeO$_3$ perovskite (Leinenweber et al. 1994).

72   Early high P-T experiments reported that FeGeO$_3$ decomposed into Fe$_2$GeO$_4$ (spinel) +

73 GeO$_2$ (rutile) at 1 GPa and 973 K (Ringwood and Seabrook 1963) and FeO (rocksalt) + GeO$_2$

74 (rutile) at 25 GPa and 1273 K (Liu 1977). However, at lower temperatures (638 K) Hattori et al

75 (2001) observed that FeGeO$_3$(II) transformed into the hexagonal ilmenite ($R\bar{3}$) structure at

76 21 GPa. The ilmenite phase has also been synthesized by heating clinopyroxene to 623 - 973 K

77 at 23.5 GPa (Nakatsuka et al. 2013). No high pressure-temperature experiments above 25 GPa

78 have been reported yet. To better understand this system, we have carried out studies of the high-

79 pressure, high-temperature behavior of FeGeO$_3$ over a wide P-T range extending beyond 1 Mbar.

80 **Experimental details**

81   FeGeO$_3$ clinopyroxene was synthesized using a stoichiometric mixture of Fe (Alfa Aesar,

82 >99.998 % purity), Fe$_2$O$_3$ (Alfa Aesar, >99.5% purity) and GeO$_2$ (Aldrich, >99.998% purity)

83 (Hattori et al. 1999; Redhammer et al. 2012). The sample was ground under ethanol and pressed

84 into a pellet using a hydraulic press (0.5 ton). The pellet was then transferred to vacuum sealed

85 silica tubes and heated at 1023 K for 72 hours. It was then re-ground and pressed and sealed

86 again and put back in the furnace at 1123 K for 12 days. After 12 days, it was examined using X-

87 ray diffraction and weak staring materials peaks were observed. Therefore, it was re-heated for 5

88more days. The final run products were re-examined by X-ray diffraction and confirmed to be

89*C2/c* clinopyroxene structure with no evidence for other phases. The calculated lattice parameters

90(a = 9.7873 (12) Å, b = 9.1323 (14) Å, c = 5.1949 (7) Å, β = 101.804 ° (11)) are in good

91agreement with previous results (Hattori et al. 1999).

92   High pressure-temperature X-ray diffraction experiments on $FeGeO_3$ were preformed

93using laser-heated diamond anvil cells (DACs). The sample was mixed with 10% Au (by

94weight), ground to ~µm grain size, and loaded into the sample chamber of a rhenium gasket in a

95symmetric DAC. The gaskets were preindented to ~30-µm thickness and ~50 to 100-µm

96diameter holes were laser drilled to form the sample chamber. Samples were compressed in cells

97with either 100-µm or 200-µm culet diamond anvils. Experimental runs were carried out both

98with and without a neon pressure transmitting medium. Neon was loaded into the sample

99chamber using a gas-loading system at the GSECARS sector of the Advanced Photon Source

100(APS). Ruby balls were used to support the sample during loading so that Ne can flow

101underneath and around the sample. In the case of experiments without a pressure medium, the

102entire gasket hole was filled with the sample + Au mixture. Table 1 summarizes the loading

103configurations of the different samples.

104   *In situ* synchrotron X-ray diffraction was carried out at beamline 13-ID-D of the APS

105using a monochromatic X-ray beam (λ = 0.3344 Å). The incident X-rays were focused with

106Kirkpatrick-Baez mirrors to dimensions of ~3 µm x 3 µm. Diffraction patterns were collected

107using a 2D detector (MAR CCD). The detector orientation was calibrated using a lanthanum

108hexaboride (LaB_6) standard. The 2D images were integrated to produce conventional one-

109dimensional diffraction patterns using DIOPTAS (Prescher and Prakapenka 2015). High-

110temperature was achieved by heating the sample from both sides with diode pumped fiber lasers

111with ~15 μm spot size (Prakapenka et al. 2008). Temperatures were measured from both sides

112using spectroradiometry (Jephcoat and Besedin 1996). The laser power was adjusted

113independently so that the temperature differences between the two sides was less than 100 K.

114Pressure was determined using the thermal equation of state (EOS) of gold (Fei et al. 2007). Peak

115positions were obtained by fitting background-subtracted Voigt line shapes to the data. Lattice

116parameters were calculated using least-squares refinement of the fitted peak positions (Holland

117and Redfern 1997).

118   LeBail and Rietveld refinements were carried out on selected data using GSAS/ EXPGUI

119(Toby 2001). The background was initially fit manually using a Chebyshev polynomial (8 terms),

120but refined at later stages. For each step, the parameters for all the observed phases were initially

121refined separately and then simultaneously. In the first step, we refined only the phase fractions

122and lattice parameters. For GeO_2 phases, the unit cell dimensions obtained from least squares

123refinement of the peak positions and atomic positions from Shiraki et al. (2003) were used as

124initial values. Then the profile function (Pseudo-Voigt with Finger-Cox-Jephcoat asymmetry and

125Stephens anisotropic strain broadening) was refined and finally the atomic positions. The

126isotropic displacement parameters (U_{iso}) were not refined.

127**Results**

128*Room-Temperature Compression*

129      $FeGeO_3$ clinopyroxene was initially compressed at room temperature to a peak pressure

130of 33 GPa, 54 GPa and 123 GPa in three separate experiments (Figure 1). Up to 11 GPa, the

131diffraction pattern can be indexed using the ambient-pressure cpx (*C2/c*) structure. Upon further

132compression to 18 GPa, the diffraction pattern changes indicating a structural phase transition

133(Figure 1a). The measured pattern can be fit using the triclinic unit cell of $FeGeO_3(II)$ ($P\acute{1}$)

134reported at 20.1 GPa by Hattori et al. (2001). Figure 2 shows a Le Bail refinement of our

135diffraction pattern at 20.4 GPa. The lattice parameters obtained from our refinement ($a = 6.7831$

136(8) Å, $b = 8.4799(11)$ Å, $c = 4.8921(5)$ Å, $\alpha = 88.717(8)°$, $\beta = 89.464(8)°$, $\gamma = 137.670(3)°$) are in

137good agreement with those of Hattori et al. (2001) ($a = 6.829$ (26) Å, $b = 8.490$ (33) Å, $c =$

1384.887(3) Å, $\alpha = 88.94(13)°$, $\beta = 89.40(13)°$, $\gamma = 137.49(16)°$). The observed pattern cannot be

139indexed using other known high-pressure structures in pyroxenes including the HP- $P2_1/c$

140clinopyroxene ($FeSiO_3$, (Pakhomova et al. 2017) or β-diopside (Plonka et al. 2012).

141   In our initial experiment (S1), $FeGeO_3$ (II) was found to remain stable to 33 GPa, the

142peak pressure reached in this sample at ambient temperature (Figure 1a). A second sample (S2)

143was prepared and compressed directly to 41 GPa at room temperature. The diffraction pattern

144for this sample appears to be identical with FeGeO3 (II) although the peaks are somewhat

145broader and there are some differences in peak intensity (Figure 1b). This may be due to

146differing amounts of non-hydrostatic stress and preferred orientation in the two samples. The

147$FeGeO_3$ (II) phase appears to remain stable to at least 54 GPa, the maximum pressure reached on

148this sample at 300 K.

149   A third sample (S3) was prepared and compressed at room temperature in two steps to 86

150GPa and then 123 GPa. Changes in the diffraction pattern indicate that an additional phase

151transformation to $FeGeO_3$ (III) occurs between 54 and 86 GPa and is maintained to 123 GPa

152(Figure 1b). Determination of the structure of $FeGeO_3$(III) was not possible from the powder

153diffraction data. Unlike the first two samples which contained a neon pressure medium, the third

154sample was compressed without a pressure transmitting medium. The broad observed diffraction

13
14

155peaks may therefore reflect a combination of a high degree of non-hydrostatic stress along with

156partial disordering of the sample. Nevertheless, it appears that $FeGeO_3$ remains largely

157crystalline to the highest pressure (123 GPa) at 300 K and does not undergo complete pressure-

158induced amorphization.

159   Earlier reported the appearance of perovskite at 33-40 GPa upon room-temperature

160compression of $FeGeO_3$ (Nagai et al. 1998; Hattori et al. 1999). Our diffraction data at 41 GPa (Figure 1b) cannot

161be indexed by the perovskite unit cell (a = 4.93 (2) Å, b = 5.06 (6) Å, c = 6.66 (3) Å at 40 GPa)

162reported by those authors. Table 1 compares the d-spacings for our pattern with those of Hattori

163et al. (1999). The difference between the two are large and rules out the perovskite phase. The

164heating runs described below also do not support the existence of the perovskite phase in this

165system.

166***High-Temperature Phase Stability***

167   Laser heating experiments were carried out at pressures of 33, 54 and 123 GPa. In each

168case, the sample was first compressed to the target pressure at room temperature and then heated.

169Each experiment involved a fresh, previously unheated sample. The pressures were chosen to

170cover the stability fields of high-pressure phases of germanium oxide. GeO_2 exhibits extensive

171polymorphism under compression (Micoulaut et al. 2006). At ambient conditions, GeO_2

172crystallizes in the rutile structure (*P4$_2$/mnm*). On compression to ~ 25 GPa, it transforms to the

173$CaCl_2$-type structure (*Pnnm*) (Haines et al. 2000). Upon further compression to ~ 44 GPa and 70

174– 90 GPa, it forms the α-PbO_2-type (*Pbcn*) and pyrite-type (*Pa* $\bar{3}$) structures, respectively (Ono

175et al. 2003a; Prakapenka et al. 2004)

15
16

176	Sample S1 was directly compressed to 33 GPa at room temperature and then heated from

177 1400 K to ~2120 K in steps of ~200 K. Figure 3a shows the X-ray diffraction pattern obtained

178 during heating to the peak temperature (*in situ* P = 39.1 GPa, including thermal pressure). All

179 major peaks can be assigned to GeO_2 (rutile- type) + FeO (B1 rocksalt-type phase). The $CaCl_2$-

180 type phase of GeO_2 is a high-pressure orthorhombic distortion of the ambient-pressure tetragonal

181 rutile-type phase (Haines et al. 2000). The phase transition can be identified from the splitting of

182 the *hkl* diffraction lines ($h \neq k$). At room temperature, the rutile-$CaCl_2$ phase transition pressure

183 has been reported to occur at 25-27 GPa (Haines et al. 1998, 2000; Ono et al. 2002) .

184 (Prakapenka et al. 2004) observed the $CaCl_2$-type phase at 36 GPa and 1600 $\pm$ 100 K. Ono et

185 al. (2002) reported that the phase boundary has a positive Clapeyron slope given by:

186
$$P(GPa) = (34.9 \pm 1.2) + (0.0086 \pm 0.0024) x (T - 1300)(K)(1)$$

187	At the peak temperature of our experiment (P, T = 39.1 GPa, 2120 K), the splitting of the

188 (211) and (121) peaks is not evident. The full width at half maximum (FWHM) of the (211) peak

189 is also comparable to other peaks for which splitting is not expected ($h = k$). These observations

190 suggest our sample remains in the rutile phase under these conditions or that we are so close to

191 the boundary that the splitting of the $CaCl_2$-type phase cannot be detected as yet. At 2120 K, the

192 phase boundary relationship (Eqn. 2) predicts a transition pressure of 41.9 $\pm$ 3.2 GPa, which is

193 consistent with our evidence for persistence of the rutile-type phase. The lattice parameters

194 obtained from least squares fitting of the peaks are a = 4.2462 (17) Å, c = 2.8122 (23) Å. The

195 calculated volume (50.707 (42) Å^3) is in general agreement with that reported by Ono et al.

196 (2002) (50.23 Å^3 at 39.7 GPa and 2050 K). The lattice parameter of the B1-type FeO (4.1431

197 (12) Å) is about 1% larger than the predicted unit cell dimension (a = 4.10 Å at 39 GPa, 2120 K)

198based on the equation of state parameters reported by Fischer et al. (2011). Tables 2a and 2b

199show the observed and calculated *d*-spacings for the rutile-type phase of GeO_2 and B1-type FeO

200at high P-T. The differences ($\Delta d = d_{obs} - d_{calc}$) are less than 0.004 Å indicating a good fit to our

201observations. In all cases lattice parameters obtained from peak fitting were used as the starting

202guesses for whole profile Rietveld refinement. The values obtained from the two methods are in

203good agreement with each other and therefore only the Rietveld refinement results have been

204reported for the remaining experiments. The unit cell dimensions and atomic positions obtained

205from Rietveld refinement are listed in Table 3.

206   On quenching to room temperature (P, T = 33.9 GPa, 300 K), the splitting of the (211)

207and (121) peaks became distinct (inset, Figure 3b). The lattice parameters of the $CaCl_2$-type

208phase (Table 3) are in good agreement with those of Prakapenka et al. (2004) (*a* = 4.2617(4) Å, *b*

209= 4.1268(2) Å, *c* = 2.7817(4) Å at 36 GPa) and Haines et al. (2000) (*a* = 4.2866(6) Å, *b* =

2104.1742(6) Å, *c* = 2.7995(2) Å at 32 GPa). The calculated volume (49.679 (45) Å^3) is also in

211agreement with Ono et al. (2002) (50.11 Å^3 at 30.7 GPa and 300 K). The rhombohedral (

212 $R\bar{3}m\lambda$ rB1 phase of FeO is identified from the splitting of the cubic (111) peak into the

213rhombohedral 003 and 101 peaks (Mao et al. 2002). In $Fe_{0.947}O$, the cubic-rhombohedral

214phase transition was observed at 18 GPa at room temperature using single crystal X-ray

215diffraction (Shu et al. 1998). In agreement with Wicks et al. (2015), we observe a mixture of the

216cubic and rhombohedral phases on quenching to room temperature. The *c/a* ratio of the

217rhombohedral phase (2.621) is consistent with Shu et al. (1998) ($Fe_{0.947}O$, 2.6362 at 30.6

218GPa) and (Jacobsen et al. 2005) ($Fe_{0.93}O$, 2.619 at 35.3 GPa). The difference between our B1

 19
 20

219lattice parameter and that obtained from the EOS parameters of Fischer et al. (2011) is less than

2201%. The atomic positions of both rutile and CaCl$_2$-type phases of GeO$_2$ are in fair agreement

221with existing literature (Haines et al. 2000; Shiraki et al. 2003).

222 As already mentioned, the pressure intervals for laser-heating were chosen such that they

223fall in the stability fields of different phases of GeO$_2$ i.e. rutile, CaCl$_2$-type, α-PbO$_2$ and pyrite-

224type. For the next sample (S2), we first increased the pressure up to 54 GPa at room temperature.

225On heating the sample to 2000 K (*in situ* P = 58.3 GPa), we observe that FeGeO$_3$ dissociated into

226a mixture of α-PbO$_2$-type GeO$_2$ and B1-type FeO within 5 minutes (Figure 4). The CaCl$_2$-type to

227α-PbO$_2$-type transition has been reported to occur at 44 GPa and 1600 ± 100 K (Prakapenka et al.

2282004). Ono et al. 2003 found the phase boundary between CaCl$_2$ and α-PbO$_2$ also has a positive

229Clapeyron slope:

230 $$P(GPa) = (53.3 \pm 3) + (0.011 \pm 0.005) x (T - 1800)(K) (2)$$

231 At 2000 K, the predicted transition pressure of 55.5 ± 4 GPa supports our observation

232of the α-PbO$_2$ phase at 58 GPa. Table 3 shows the structural parameters of the oxide assemblage

233obtained from Rietveld refinement. The unit cell dimensions of GeO$_2$ are in agreement with

234those of (Prakapenka et al. 2003)(*a* = 4.0423(8) Å, *b* = 5.0396(8) Å, *c* = 4.5288(0) at 60 GPa,

2351800 K).

236 Finally, we compressed FeGeO$_3$ (S3) to a pressure of 123 GPa at room temperature and

237heated it from ~1200 to ~ 1700 K (Figure 5). This experiment did not have any pressure-

238transmitting (insulating) medium. The diffraction pattern at the peak P, T condition (127.3 GPa

239and1700 K) can be indexed using GeO$_2$ (pyrite-type) and FeO (B1) (Table 3) again indicating the

240dissociation of FeGeO$_3$ at high-pressures. Our observation of the pyrite phase at this pressure and

241temperature is consistent with previous observations that this phase can be synthesized by laser

242heating to 1900 K above 100 GPa (Ono et al. 2003b). The unit cell dimension and atomic

243positions of pyrite-type GeO_2 are in good agreement with those reported by (Shiraki et al. 2003)

244((a = 4.3365 (15) Å at 108 GPa).

245Discussion

246   The behavior of $FeGeO_3$ under compression has been clarified by this study. $FeSiO_3$ has

247been observed in three polymorphic forms at ambient conditions: ferrosilite (orthpyroxene,

248*Pbca*), clinoferrosilite ($P2_1/c$) and a triclinic pyroxenoid form ($P\bar{1}$ ¿ (Lindsley et al.

2491964; Weber 1983). In room temperature single-crystal compression studies, clinoferrosilite

250undergoes a phase transition to the *C2/c* clinopyroxene (cpx) structure between 1.3 and 3.0 GPa

251(Hugh-Jones et al. 1994; Pakhomova et al. 2017) and then into another high-pressure monoclinic

252phase (HP- $P2_1/c$) between 30 – 36 GPa (Pakhomova et al. 2017). In addition, single-crystal

253studies have investigated high-pressure phase transitions for various other compositions in the

254(Mg,Fe)SiO_3 system (Zhang et al. 2013; Dera et al. 2013; Finkelstein et al. 2015). In contrast,

255$FeGeO_3$ crystallizes in the high-pressure *C2/c* cpx structure, which remains stable up to ~18 GPa.

256Under room temperature compression, it undergoes two phase transitions at ~ 18 GPa

257($FeGeO_3$(II)) and in between 54-86 GPa ($FeGeO_3$(III)). $FeGeO_3$ (III) was found to remain stable

258up to ~123 GPa.

259   At high temperatures, $FeGeO_3$ and $FeSiO_3$ show similar behavior. The Fe endmember

260compositions in these systems are distinct from intermediate iron-bearing compositions. In the

261(Mg,Fe)SiO_3 system, perovskites and post-perovskites have been synthesized with Fe# up to 0.8

262(Mao et al. 2004). In germanates, compositions with Fe# ≤ 22, single phase pv and ppv was

263observed, while compositions with Fe# > 22, evidences for partial decomposition were found

264(Stan et al. 2017). As already mentioned, experimental studies have reported that the Pv and pPv

265phases are not stable in $FeSiO_3$. Instead, a mixture of FeO (B1 phase) and a high-pressure SiO_2

266phase was found in experiments covering a wide pressure range up to 149 GPa (Fujino et al.

2672009). In this study, we have shown that $FeGeO_3$ behaves similarly and breaks down into GeO_2 +

268FeO at least up to 1.27 Mbars.

269   Further understanding of the behavior of FeGeO3 relative to other analogs can by obtain

270by consideration of the the Goldschmidt diagram. This type of diagram has been commonly used

271to predict the stability of the perovskite and post-perovskite structures in ABO_3 compounds

272(Goldschmidt 1926; Hattori et al. 1999; Fujino et al. 2009; Tateno et al. 2010) (Figure 6). The

273Goldschmidt tolerance factor, *t,* can be used to assess the potential stability of the two phases. It

274is calculated from the ionic radii of the eightfold-coordinated A cation (R_A), sixfold-

275coordinated B (R_B) cation and the ionic radius of the oxygen anion (R_O) as given by:

276        $t = \dfrac{R_A + R_O}{\sqrt{2}\left(R_B + R_O\right)} (3)$ Compounds with 0.75 < *t* < 1.0 favor the perovskite structure (Ito

277and Matsui 1979; Tateno et al. 2010). A perovskite structure has been predicted to be stable for

278all the compounds shown in Figure 6. It is further observed that high-pressure perovskite phases

279with *t* > 0.84 are generally quenchable and the ones with *t* < 0.84 are not (Leinenweber et al.

2801994).

281   Based on Goldschmidt criteria, the Fe end-members $FeSiO_3$ ($t = 0.91$), $FeGeO_3$ ($t = 0.85$),

282and $FeTiO_3$ ($t = 0.82$) should all adopt the perovskite structure (Sato et al. 1991; Haines and

283Léger 1993; Wilson et al. 2005). The perovskite phase of $FeTiO_3$ has been synthesized from the

284$LiNbO_3$-type structure at 16 GPa (Leinenweber et al. 1991) and from the ilmenite phase on

285heating at 20 GPa and 973 K (Ming et al. 2006). However, $FeSiO_3$ appears to be an exception to

286the Goldschmidt criterion as experimental studies indicate it does not transform to the perovskite

287structure (Fujino et al. 2009).

288   It has been observed that the tolerance factors of reported post-perovskites are less than

2890.90 (Bremholm et al. 2011). By this criterion, $FeTiO_3$ should form post-perovskite. Theoretical

290calculations also predict both Pv and pPv to be stable (Wilson et al. 2005). However, it was

291found experimentally that $FeTiO_3$ perovskite dissociates from perovskite into $\left(Fe_{1-x} Ti_x O \right)$ +

292$\left(Fe_{1+x} Ti_{2-x} O_5 \right)$ at 53 GPa and 2000 K (Wu et al. 2011) or $\left(Fe_{1-x} Ti_{0.5x} O \right)$ + $Fe Ti_3 O_7$

293at 42 GPa and 2000 K (Nishio-Hamane et al. 2010). The absence of post-perovskite in titanates

294(Tateno et al. 2006) has been attributed to the increase in the coordination number of Ti^{4+} to

295seven (compared with six in both perovskite and post-perovskite) at relatively low-pressures

296(Sato et al. 1991; Haines and Léger 1993).

297   In case of the germanate system, $MgGeO_3$, $MnGeO_3$ and $ZnGeO_3$ form pPv upon heating

298to ~63 GPa (Hirose et al. 2005), ~60 GPa (Tateno et al. 2006) and ~115 GPa (Yusa et al. 2014)

299respectively. Post-perovskite has not been observed in $CaGeO_3$ (Nakatsuka et al. 2015) and

300$CdGeO_3$ (Tateno et al. 2006), which is also expected as t > 0.90 for both. In the case of $FeGeO_3$,

301tolerance factor considerations suggest that both perovskite and post-perovskite should be stable.

302However, our experimental results show that, in contrast to earlier studies (Nagai et al. 1998;

27
28

303Hattori et al. 1999), neither of these phases form in $FeGeO_3$ up to 127 GPa. Thus, the

304Goldschmidt criteria are not applicable to the Fe endmembers of the $(Mg,Fe)SiO_3$ and

305$(Mg,Fe)GeO_3$ systems. This can be explained by the crystal field stabilization energy (CFSE) of

306transition metals with unfilled 3d electrons (6 for Fe^{2+}) in the octahedral coordination of B1/rB1

307structure in comparison to the dodecahedral perovskite site (Burns 1993; Fujino et al. 2009).

308Estimates indicate that octahedrally coordinated Fe^{2+} has a higher CFSE than 8-coordinated Fe^{2+}

309(e.g. CFSE of Fe^{2+} in magnesiowüstite exceeds that of Fe^{2+} in the perovskite structure by ~56

310KJ/mole). In case of $MnGeO_3$ and $MnSiO_3$ the filled 3d electrons (5 for Mn^{2+}) lead to no CFSE,

311thereby making the perovskite structure stable. We also find no evidence for the formation of

312other phases as suggested from first-principles calculations (Cohen and Lin, 2014).

313　　　　There has been interest in understanding the behavior of the $(Mg,Fe)SiO_3$ system at

314ultrahigh pressures (Duffy et al. 2015).   Theoretical studies indicate that $MgSiO_3$ will dissociate

315into CsCl-type MgO and cotunnite-type SiO_2 at 11.2 Mbar (Umemoto et al. 2006). However, no

316studies have examined Fe-bearing compositions in this system at ultrahigh pressures as yet. Our

317experiments show that $FeGeO_3$ dissociates into oxides across the stability fields of the α-PbO2

318and pyrite-type phases of GeO_2. In SiO_2, these phases are expected to have stability ranges from

319121 – 268 GPa (Murakami et al. 2003; Kuwayama et al. 2005) and 200-690 (Tsuchiya and

320Tsuchiya 2011) GPa, respectively. Applying our results to the silicate system suggests that the

321breakdown of $FeSiO_3$ would be expected to extend to pressures as high as 690 GPa. Theoretical

322studies of Fe-bearing compositions remain challenging and analog materials can provide a useful

323benchmark for such calculations (Shukla et al. 2015). Future studies of intermediate

324compositions in the $(Mg,Fe)GeO_3$ system may provide further constraints on the ultrahigh

325pressure behavior of this system.

326 Conclusions

327        $FeGeO_3$ clinopyroxene undergoes a pressure-induced phase transition at ~18 GPa at room

328 temperature. The diffraction pattern is consistent the $FeGeO_3$ (II) structure. On increasing the

329 pressure, the diffraction peaks broaden and there is evidence for another phase transition between

330 54 and 86 GPa. This phase remains stable at room temperature up to 123 GPa, the peak pressure

331 considered here. In contrast to previous studies, we did not find any evidence of formation of

332 perovskite at ~ 40 GPa and 300 K. On laser heating at 33, 54 and 123 GPa, $FeGeO_3$ dissociated

333 into a mixture of GeO_2 (rutile/ $CaCl_2$, α-PbO_2 and pyrite-type respectively) and FeO (B1/ B1 +

334 rB1). The structural parameters of the oxide phases at different pressures were calculated using

335 both least squares peak fitting and Rietveld refinement. Our calculated unit cell dimensions and

336 atomic coordinates are in good agreement with existing literature. In contrast to predictions

337 based on ionic ratios, the perovskite or post-perovskite phases are not formed in $FeGeO_3$ to

338 pressures above 1 Mbar. This result is consistent with findings for $FeSiO_3$ and suggest that

339 $FeSiO_3$ breakdown will persist to ~700 GPa.

340 Acknowledgements

References

Badro J (2014) Spin transitions in mantle minerals. Annu Rev Earth Planet Sci 42:231–248.

Bremholm M, Dutton SE, Stephens PW, Cava RJ (2011) NaIrO3—A pentavalent post-perovskite. J Solid State Chem 184:601–607.

Burns RG (1993) Mineralogical applications of Crystal Field Theory. Cambridge University Press.

Cohen RE, Lin Y (2014) Prediction of a potential high-pressure structure of $FeSiO_3$. Phys Rev B 90:140102.

Dera P, Finkelstein GJ, Duffy TS, et al (2013) Metastable high-pressure transformations of orthoferrosilite Fs_{82}. Phys Earth Planet Inter 221:15–21.

Dorfman SM, Meng Y, Prakapenka VB, Duffy TS (2013) Effects of Fe-enrichment on the equation of state and stability of $(Mg,Fe)SiO_3$ perovskite. Earth Planet Sci Lett 361:249–257.

Dorfman SM, Shieh SR, Meng Y, et al (2012) Synthesis and equation of state of perovskites in the $(Mg,Fe)_3Al_2Si_3O_{12}$ system to 177 GPa. Earth Planet Sci Lett 357–358:194–202.

Duffy T, Madhusudhan N, Lee KKM (2015) Mineralogy of super-earth planets. In: Schubert G (ed) Treatise on Geophysics (Second Edition). Elsevier, Oxford, pp 149–178

Fei Y, Ricolleau A, Frank M, et al (2007) Toward an internally consistent pressure scale. Proc Natl Acad Sci 104:9182–9186.

Finkelstein GJ, Dera PK, Duffy TS (2015) Phase transitions in orthopyroxene (En90) to 49 GPa from single-crystal X-ray diffraction. Phys Earth Planet Inter 244:78–86.

Fischer RA, Campbell AJ, Shofner GA, et al (2011) Equation of state and phase diagram of FeO. Earth Planet Sci Lett 304:496–502.

Fujino K, Nishio-Hamane D, Suzuki K, et al (2009) Stability of the perovskite structure and possibility of the transition to the post-perovskite structure in $CaSiO_3$, $FeSiO_3$, $MnSiO_3$ and $CoSiO_3$. Phys Earth Planet Inter 177:147–151.

Goldschmidt VM (1926) Die Gesetze der Krystallochemie. Naturwissenschaften 14:477–485.

Greenblatt M, Hornreich RM, Sharon B (1974) Evidence for a spin-reorientation type phase transition in $FeGeO_3$. Solid State Commun 14:1177–1181.

Haines J, Léger JM (1993) X-ray diffraction study of TiO_2 up to 49 GPa. Phys B Condens Matter 192:233–237.

Haines J, Léger JM, Chateau C, et al (1998) Ferroelastic phase transition in rutile-type germanium dioxide at high pressure. Phys Rev B 58:R2909–R2912.

Haines J, Léger JM, Chateau C, Pereira AS (2000) Structural evolution of rutile-type and $CaCl_2$-type germanium dioxide at high pressure. Phys Chem Miner 27:575–582.

383Hattori T, Matsuda T, Tsuchiya T, et al (1999) Clinopyroxene-perovskite phase transition of
384FeGeO$_3$ under high pressure and room temperature. Phys Chem Miner 26:212–216.

385Hattori T, Nagai T, Yamanaka T, et al (2000) Single-crystal X-ray diffraction study of FeGeO$_3$
386high-P clinopyroxene (*C2/c*) up to 8.2 GPa. Am Mineral 85:1485–1491.

387Hattori T, Tsuchiya T, Nagai T, Yamanaka T (2001) Sequential high-pressure transformations of
388FeGeO$_3$ high-P clinopyroxene (*C2/c*) at temperatures up to 365^{0}C. Phys Chem Miner 28:377–
389387.

390Hirose K, Kawamura K, Ohishi Y, et al (2005) Stability and equation of state of MgGeO$_3$ post-
391perovskite phase. Am Mineral 90:262–265.

392Holland TJB, Redfern SAT (1997) Unit cell refinement from powder diffraction data; the use of
393regression diagnostics. Mineral Mag 61:65–77.

394Hugh-Jones DA, Woodland AB, Angel RJ (1994) The structure of high-pressure *C2/c* ferrosilite
395and crystal chemistry of high-pressure *C2/c* pyroxenes. Am Mineral 79:1032–1041.

396Ito E, Matsui Y (1979) High-pressure transformations in silicates, germanates, and titanates with
397ABO$_3$ stoichiometry. Phys Chem Miner 4:265–273.

398Jacobsen SD, Lin J-F, Angel RJ, et al (2005) Single-crystal synchrotron X-ray diffraction study
399of wüstite and magnesiowüstite at lower-mantle pressures. J Synchrotron Radiat 12:577–583.

400Jephcoat AP, Besedin SP (1996) Temperature measurement and melting determination in the
401laser-heated diamond-anvil cell. Philos Trans Math Phys Eng Sci 354:1333–1360.

402Kuwayama Y, Hirose K, Sata N, Ohishi Y (2005) The pyrite-type high-pressure form of silica.
403Science 309:923–925.

404Lay T, Hernlund J, Garnero EJ, Thorne MS (2006) A post-perovskite lens and D'' heat flux
405beneath the central Pacific. Science 314:1272–1276.

406Leinenweber K, Utsumi W, Tsuchida Y, et al (1991) Unquenchable high-pressure perovskite
407polymorphs of MnSnO$_3$ and FeTiO$_3$. Phys Chem Miner 18:244–250.

408Leinenweber K, Wang Y, Yagi T, Yusa H (1994) An unquenchable perovskite phase of MgGeO$_3$
409and comparison with MgSiO$_3$ perovskite. Am Mineral 79:197–199.

410Lin J-F, Speziale S, Mao Z, Marquardt H (2013) Effects of the electronic spin transitions of iron
411in lower mantle minerals: Implications for deep mantle geophysics and geochemistry. Rev
412Geophys 51:244–275.

413Lindsley DH, Davis BTC, Macgregor ID (1964) Ferrosilite (FeSiO$_3$): Synthesis at high pressures
414and temperatures. Science 144:73–74.

415Liu L (1977) The post-spinel phases of twelve silicates and germanates. In: Manghnani MH,
416Akimoto S (eds) High-pressure research; Applications in geophysics. Academic Press, New York

417Mao W, Shu J, Hu J, et al (2002) Displacive transition in magnesiowüstite. J Phys Condens 418Matter 14:11349.

419Mao WL, Shen G, Prakapenka VB, et al (2004) Ferromagnesian postperovskite silicates in the D 420″ layer of the Earth. Proc Natl Acad Sci U S A 101:15867–15869.

421Micoulaut M, Cormier L, Henderson GS (2006) The structure of amorphous, crystalline and 422liquid GeO_2. J Phys Condens Matter 18:R753.

423Ming L-C, Bassett WA (1975) High-pressure phase transformations in the system of $MgSiO_3$- 424$FeSiO_3$. Earth Planet Sci Lett 27:85–89.

425Ming LC, Kim Y-H, Uchida T, et al (2006) In situ X-ray diffraction study of phase transitions of 426$FeTiO_3$ at high pressures and temperatures using a large-volume press and synchrotron radiation. 427Am Mineral 91:120–126.

428Murakami M, Hirose K, Ono S, Ohishi Y (2003) Stability of $CaCl_2$-type and α-PbO_2-type SiO_2 at 429high pressure and temperature determined by in-situ X-ray measurements. Geophys Res Lett 43030:1207.

431Murakami M, Hirose K, Kawamura K, et al (2004) Post-perovskite phase transition in $MgSiO_3$. 432Science 304:855–858.

433Nagai T, Hattori T, Tsuchiya T, Yamanaka T (1998) First observation of $FeGeO_3$-perovskite 434under high pressure. Solid State Commun 107:223–225.

435Nakatsuka A, Kuribayashi S, Nakayama N, et al (2015) Temperature dependence of crystal 436structure of $CaGeO_3$ high-pressure perovskite phase and experimental determination of its Debye 437temperatures studied by low- and high-temperature single-crystal X-ray diffraction. Am Mineral 438100:1190–1202.

439Nakatsuka D, Yoshino T, Kano J, et al (2013) High-pressure synthesis, crystal structure and 440magnetic property of ilmenite-type $FeGeO_3$. J Solid State Chem 198:520–524.

441Nishio-Hamane D, Yagi T, Ohshiro M, et al (2010) Decomposition of perovskite $FeTiO_3$ into 442wüstite $Fe_{1-x}Ti_{0.5x}O$ and orthorhombic $FeTi_3O_7$ at high pressure. Phys Rev B 82:092103.

443Oganov AR, Ono S (2004) Theoretical and experimental evidence for a post-perovskite phase of 444$MgSiO_3$ in Earth's D" layer. Nature 430:445–448.

445Ono S, Hirose K, Nishiyama N, Isshiki M (2002) Phase boundary between rutile-type and $CaCl_2$- 446type germanium dioxide determined by in situ X-ray observations. Am Mineral 87:99–102.

447Ono S, Tsuchiya T, Hirose K, Ohishi Y (2003a) Phase transition between the $CaCl_2$-type and α- 448PbO_2-type structures of germanium dioxide. Phys Rev B 68:134108.

449Ono S, Tsuchiya T, Hirose K, Ohishi Y (2003b) High-pressure form of pyrite-type germanium 450dioxide. Phys Rev B 68:014103.

451Pakhomova A, Ismailova L, Bykova E, et al (2017) A new high-pressure phase transition in 452clinoferrosilite: In situ single-crystal X-ray diffraction study. Am Mineral 102:666–673.

453Plonka AM, Dera P, Irmen P, et al (2012) β-diopside, a new ultrahigh-pressure polymorph of
454$CaMgSi_2O_6$ with six-coordinated silicon. Geophys Res Lett 39:L24307.

455Prakapenka VB, Dubrovinsky LS, Shen G, et al (2003) α-PbO_2-type high-pressure polymorph of
456GeO_2. Phys Rev B 67:132101.

457Prakapenka VB, Kubo A, Kuznetsov A, et al (2008) Advanced flat top laser heating system for
458high pressure research at GSECARS: application to the melting behavior of germanium. High
459Press Res 28:3 225–235.

460Prakapenka VB, Shen G, Dubrovinsky LS, et al (2004) High pressure induced phase
461transformation of SiO_2 and GeO_2: difference and similarity. J Phys Chem Solids 65:8 1537–1545.

462Prescher C, Prakapenka VB (2015) DIOPTAS: a program for reduction of two-dimensional X-
463ray diffraction data and data exploration. High Press Res 35:3 223–230.

464Redhammer GJ, Senyshyn A, Tippelt G, et al (2012) Magnetic and low-temperature structural
465behavior of clinopyroxene-type $FeGeO_3$: A neutron diffraction, magnetic susceptibility, and [57]Fe
466Mössbauer study. Am Mineral 97:694–706.

467Ringwood AE, Seabrook M (1963) High-pressure phase transformations in germanate pyroxenes
468and related compounds. J Geophys Res 68:4601–4609.

469Royen P, Forwerg W (1963) Darstellung und kristallographische Eigenschaften der
470Metagermanate des Mangans, Eisens und Kobalts. Z Für Anorg Allg Chem 326:113–126.

471Sato H, Endo S, Sugiyama M, et al (1991) Baddeleyite-type high-pressure phase of TiO_2. Science
472251:786.

473Shiraki K, Tsuchiya T, Ono S (2003) Structural refinements of high-pressure phases in
474germanium dioxide. Acta Crystallogr B 59:701–708.

475Shu J, Mao H, Hu J, et al (1998) Single-crystal X-ray diffraction of wüstite to 30GPa hydrostatic
476pressure. Neues Jahrb Für Mineral - Abh 309–323.

477Shukla G, Topsakal M, Wentzcovitch RM (2015) Spin crossovers in iron-bearing $MgSiO_3$ and
478$MgGeO_3$: Their influence on the post-perovskite transition. Phys Earth Planet Inter 249:11–17.

479Stackhouse S, Brodholt JP, Price GD (2006) Elastic anisotropy of $FeSiO_3$ end-members of the
480perovskite and post-perovskite phases. Geophys Res Lett 33:L01304.

481Stan CV, Dutta R, Cava RJ, Prakapenka VB, Duffy TS (2017) High-pressure study of
482perovskites and post-perovskites in the (Mg,Fe)GeO_3 System. Inorg Chem 56 (14) 8026-8035.

483Tateno S, Hirose K, Sata N, Ohishi Y (2007) Solubility of FeO in (Mg,Fe)SiO_3 perovskite and
484the post-perovskite phase transition. Phys Earth Planet Inter 160:319–325.

485Tateno S, Hirose K, Sata N, Ohishi Y (2010) Structural distortion of $CaSnO_3$ perovskite under
486pressure and the quenchable post-perovskite phase as a low-pressure analogue to $MgSiO_3$. Phys
487Earth Planet Inter 181:54–59.

488Tateno S, Hirose K, Sata N, Ohishi Y (2006) High-pressure behavior of $MnGeO_3$ and $CdGeO_3$ 489perovskites and the post-perovskite phase transition. Phys Chem Miner 32:721.

490Toby BH (2001) EXPGUI, a graphical user interface for GSAS. J Appl Crystallogr 34:210–213.

491Tsuchiya T, Tsuchiya J (2011) Prediction of a hexagonal SiO_2 phase affecting stabilities of 492$MgSiO_3$ and $CaSiO_3$ at multimegabar pressures. Proc Natl Acad Sci 108:1252–1255.

493Umemoto K, Wentzcovitch RM, Allen PB (2006) Dissociation of $MgSiO_3$ in the cores of gas 494giants and terrestrial exoplanets. Science 311:983–986.

495Weber H-P (1983) Ferrosilite III, the high-temperature polymorph of $FeSiO_3$. Acta Crystallogr C 49639:1–3.

497Wicks JK, Jackson JM, Sturhahn W, et al (2015) Thermal equation of state and stability of 498$(Mg_{0.06}Fe_{0.94})O$. Phys Earth Planet Inter 249:28–42.

499Wilson NC, Russo SP, Muscat J, Harrison NM (2005) High-pressure phases of $FeTiO_3$ from first 500principles. Phys Rev B 72:024110.

501Wu X, Qin S, Dubrovinsky L (2011) Investigation into high-pressure behavior of $MnTiO_3$: X-ray 502diffraction and Raman spectroscopy with diamond anvil cells. Geosci Front 2:107–114.

503Yusa H, Tsuchiya T, Akaogi M, et al (2014) Postperovskite Phase Transition of $ZnGeO_3$: 504comparative crystal chemistry of postperovskite phase transition from germanate perovskites. 505Inorg Chem 53:11732–11739.

506Zhang L, Meng Y, Dera P, et al (2013) Single-crystal structure determination of $(Mg,Fe)SiO_3$ 507postperovskite. Proc Natl Acad Sci 110(16): 6292–6295.

508Zhang L, Meng Y, Yang W, et al (2014) Disproportionation of $(Mg,Fe)SiO_3$ perovskite in earth's 509deep lower mantle. Science 344:877–882.

510

511

512Figure 1. X-ray diffraction patterns of $FeGeO_3$ compressed at room temperature. Asterisks and

513solid circles indicate the main peaks of $FeGeO_3$ (II) and $FeGeO_3$ (III) respectively. (a) Diffraction

514data recorded up to 33 GPa. The bottom-most spectrum represents the *C2/c* clinopyroxene phase

515at 1 bar. The red ticks indicate the diffraction peak locations for the calculated clinopyroxene unit

516cell with lattice parameters $a = 9.7873$ (12) Å, $b = 9.1323$ (14) Å, $c = 5.1949$ (7) Å, $\beta = 101.804$ °

517(11) (b) Diffraction data from 33 – 123 GPa. The red ticks indicate the observed diffraction peak

518positions for the perovskite unit cell reported by Hattori et al. 1999 at 40 GPa ($a = 4.93$ (2) Å, b

519$= 5.06$ (6) Å, $c = 6.66$ (3) Å). Diffraction peaks from gold (Au) and neon (Ne) are labeled.
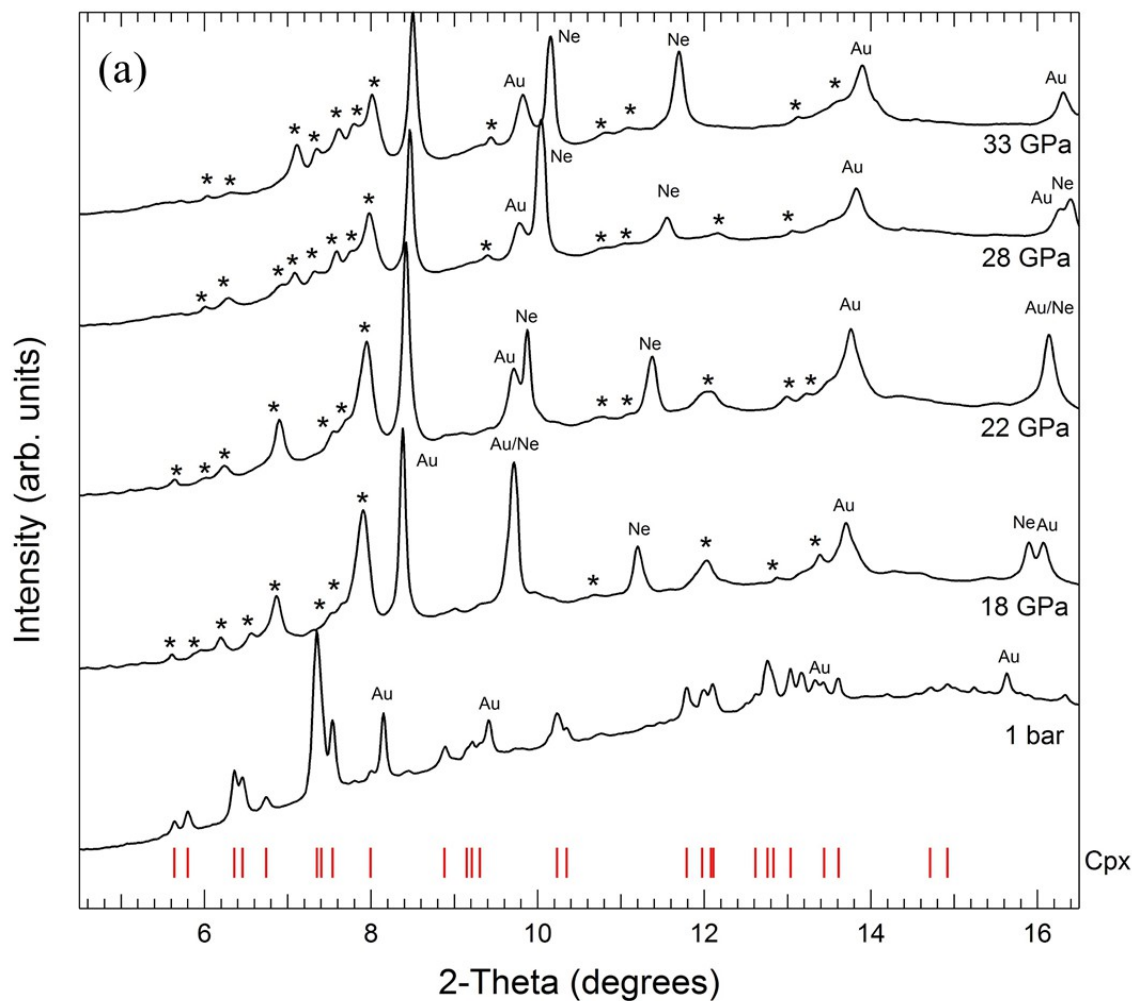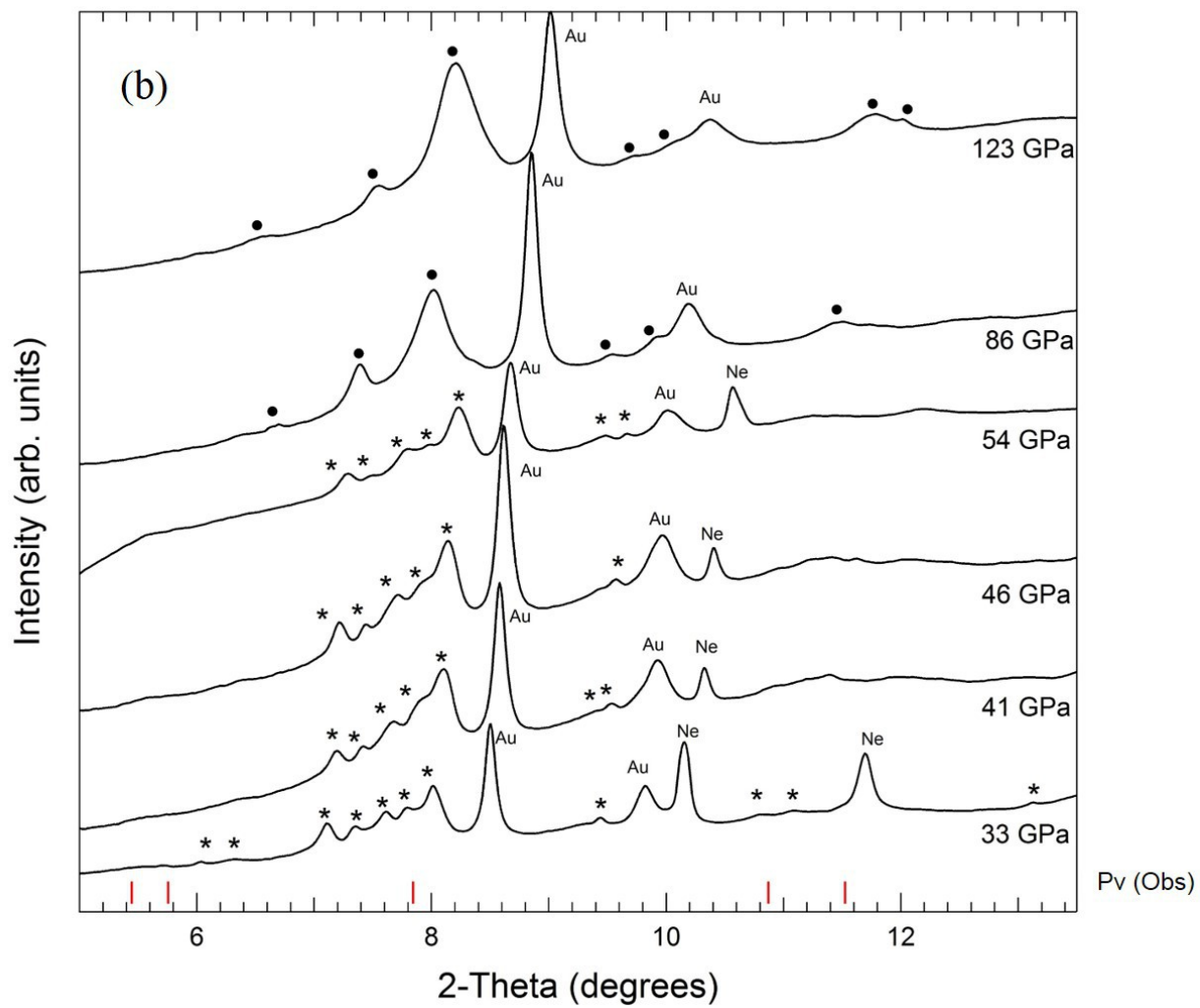

520

521

43

44

522
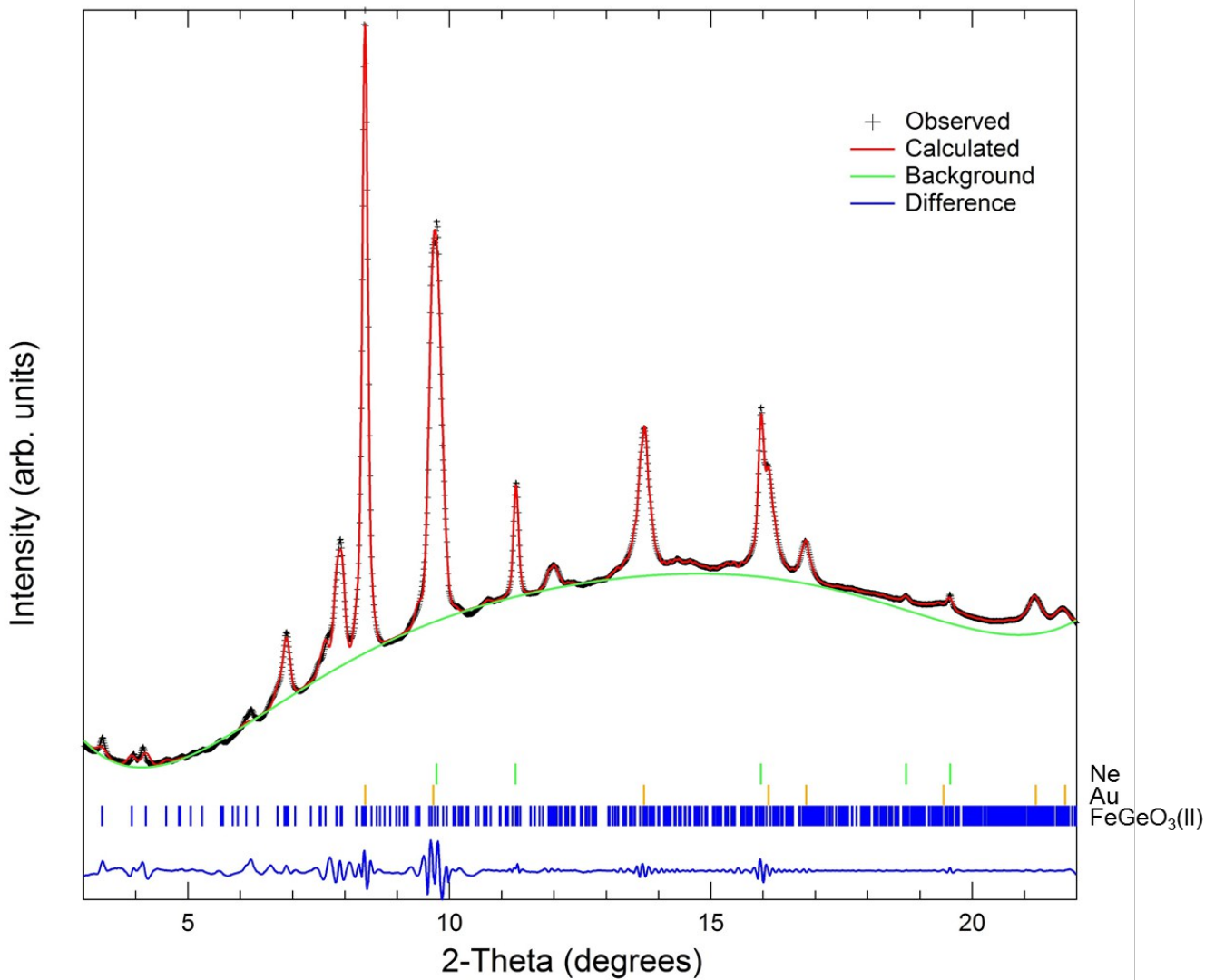
523

524

525

526

527

528

529

530

531

532Figure 2. LeBail refinement of FeGeO$_3$ (II) (Space group: $P\bar{1}$) at 20 GPa (R$_p$/R$_{wp}$ =
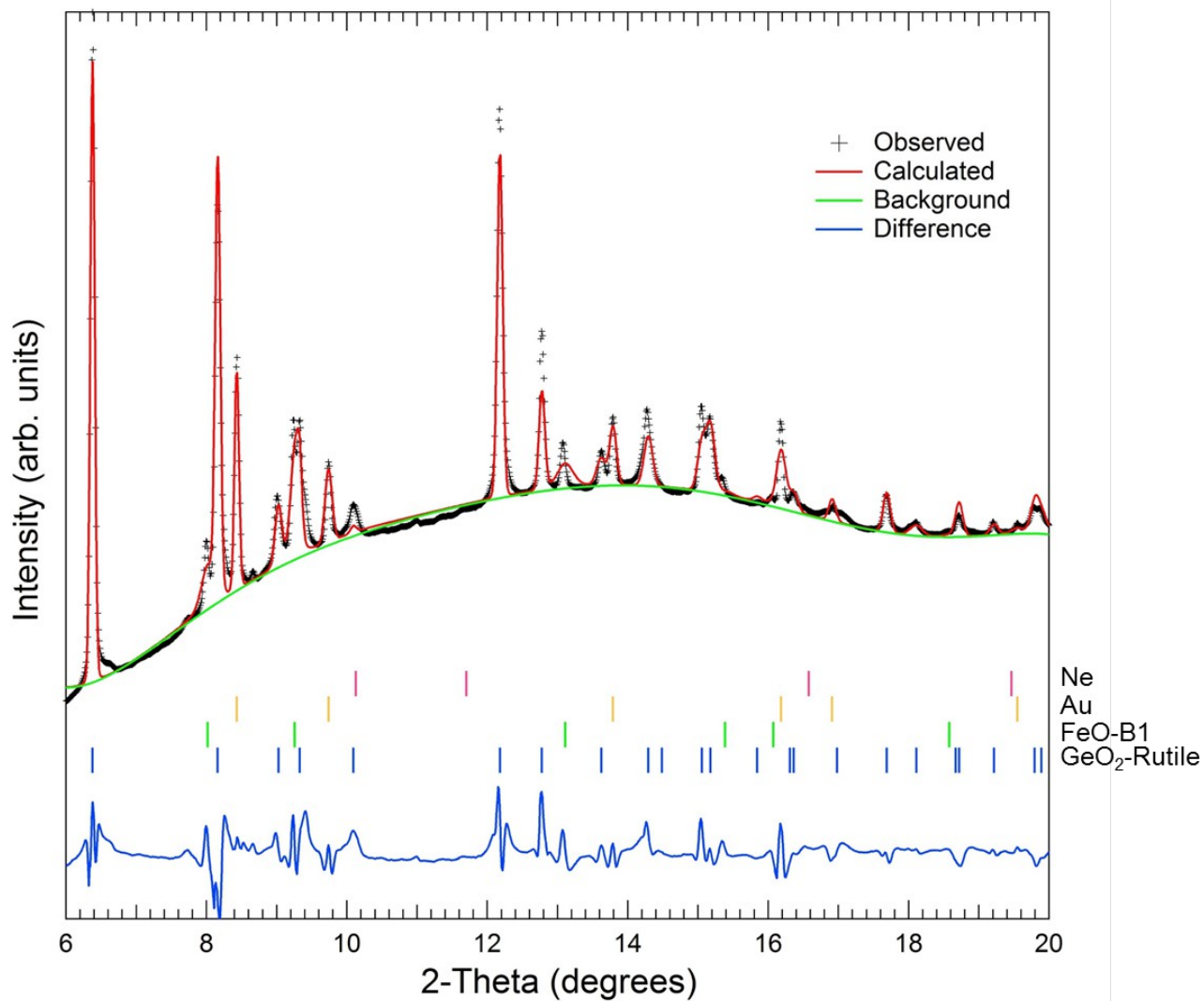
5330.0039/0.0069).

534

535

536

537

538

539Figure 3a. Rietveld refinement of the diffraction pattern obtained on heating $FeGeO_3$ to 2120 K

540at 39.1 GPa. The corresponding oxide assemblage is rutile-type GeO_2 (blue sticks) and B1-type

541FeO (green sticks).

542

543

544

545

546

547Figure 3b. Rietveld refinement of the diffraction pattern attained on quenching to room

548temperature at 33.9 GPa. The inset shows a magnified view of the splitting of the tetragonal

549(rutile) 211 peak into the orthorhombic (CaCl$_2$) 211 and 121 peaks. The blue sticks show the

550predicted peak positions of CaCl$_2$-type GeO$_2$, while light and dark green represent rhombohedral

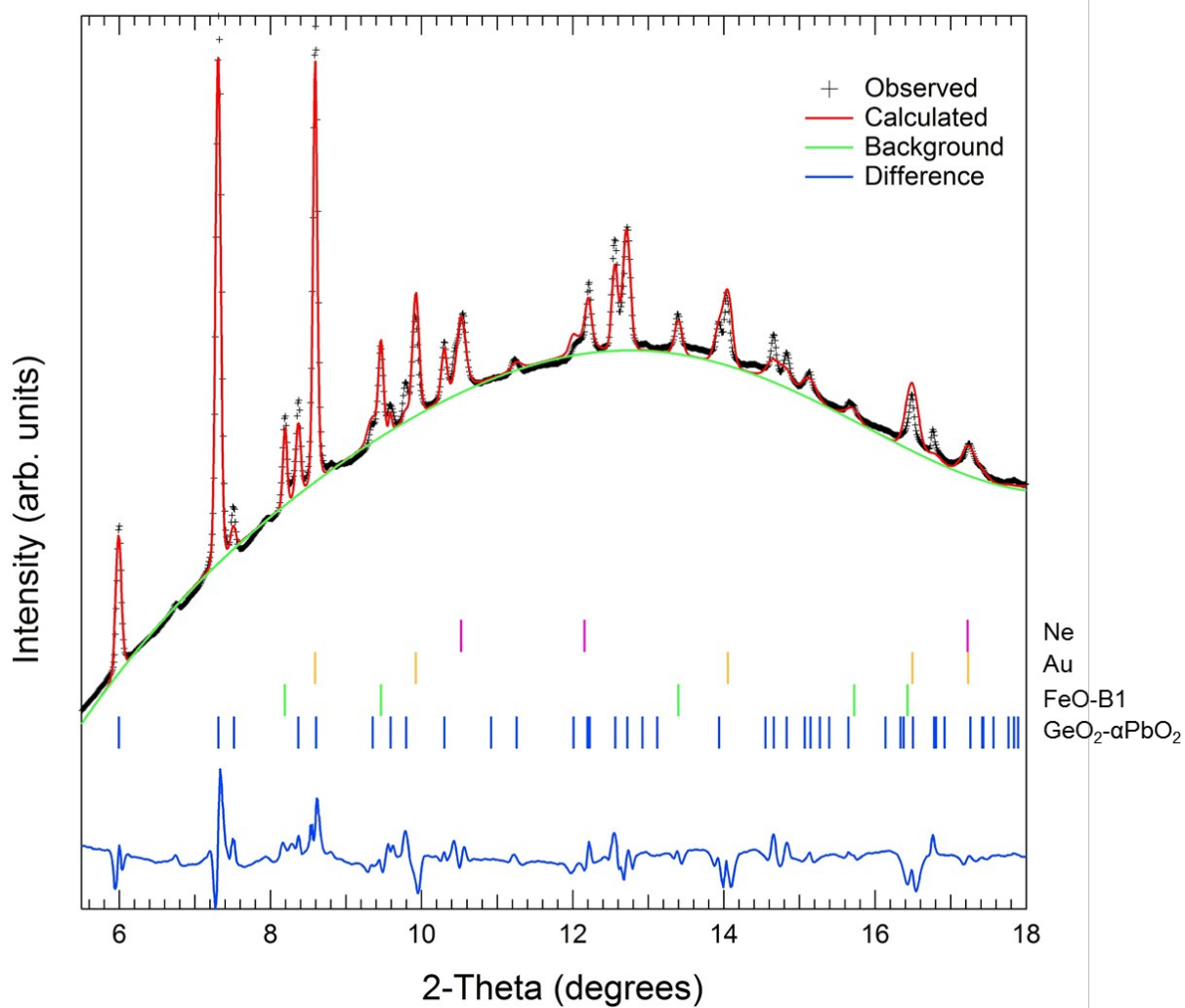551(rB1) and cubic (B1) FeO.

53
54

27
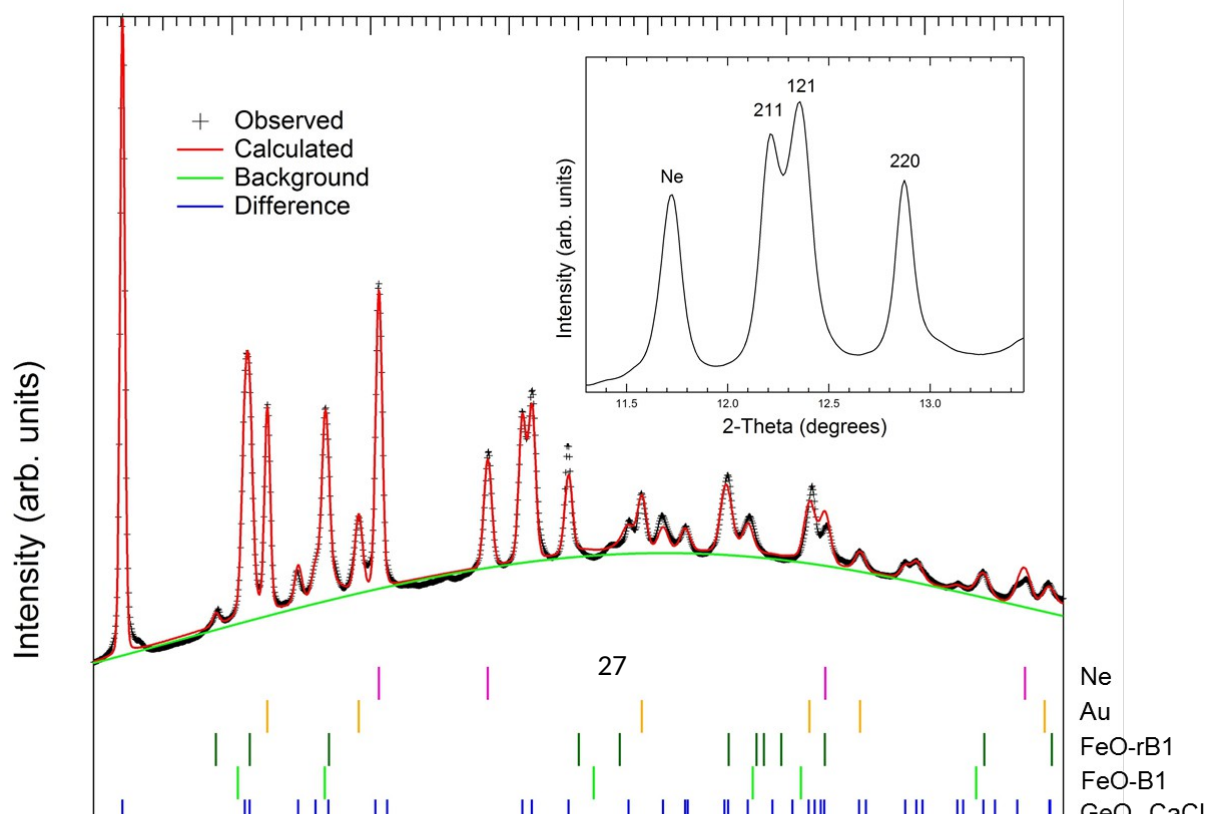
553

554

555

556Figure 4. Rietveld refinement of the x-ray diffraction pattern at 58.3 GPa and 2000 K. The

557spectrum can be indexed by GeO$_2$ (α-PbO$_2$-type), FeO (B1-type), Au, and Ne.
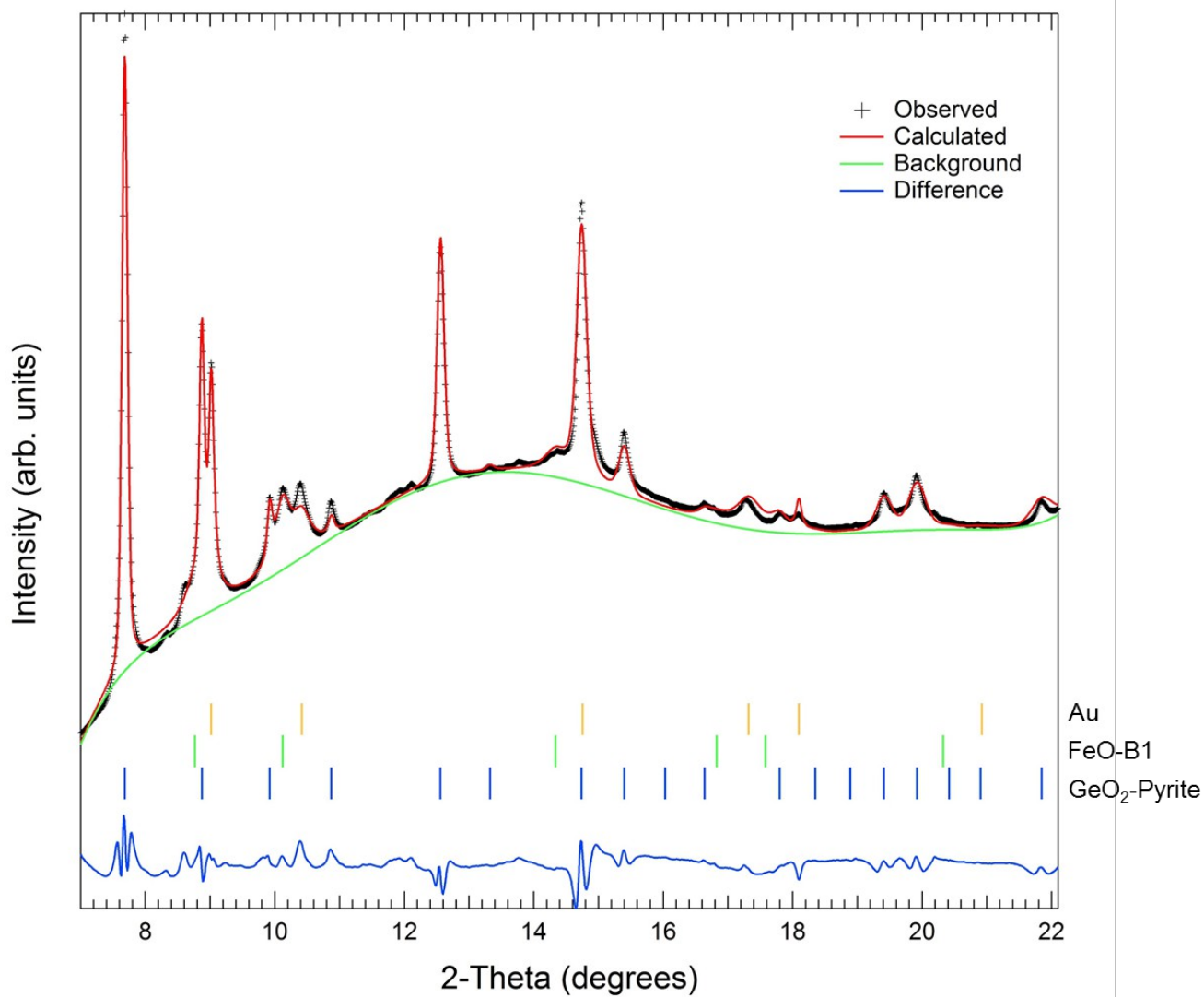
558

559

560

561

562

563

564

565Figure 5. Rietveld refinement of the diffraction pattern obtained on heating $FeGeO_3$ to 1700 K at

566127.3 GPa. The oxide assemblage consists of pyrite-type GeO_2 and B1-type FeO.

567

568

569

570

571

572

573

574Figure 6. Goldschmidt diagram of $A^{2+}B^{4+}O_3$ compounds showing compositions for which the

575perovskite structure is predicted to be stable. (after Fujino et al. 2009). The dashed lines indicate

576tolerance factor values (t). The solid line (t=0.90) delineates the boundary above which pPv is

577generally not observed. Solid circles: compounds that adopt the post-perovskite structure; red

578crosses: compounds that have not been observed to transform to post-perovskite; open circles:

579compounds for which it is not known if post-perovskite forms.
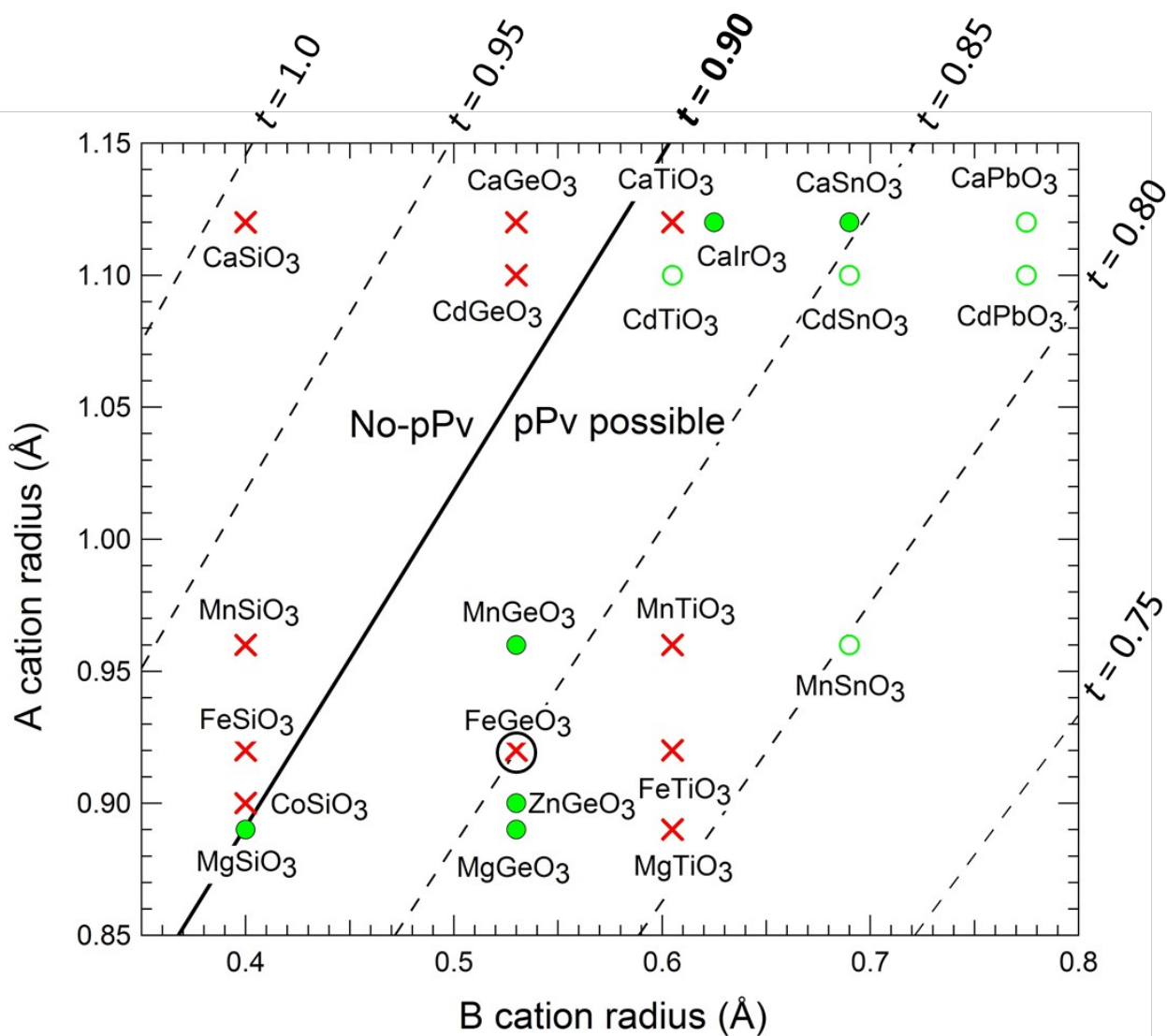
582Figure S1. P-T phase diagram of FeGeO$_3$. The solid circles represent our room temperature data

583(red: cpx, blue: FeGeO$_3$ (II), green: FeGeO$_3$(III)). The blue open circle is FeGeO$_3$(II) reported by

584Hattori et al. (2001). The solid triangles denote the high-temperature data, the bars connect the

585lowest and highest temperatures reached in that run. The black plus symbols indicate literature

586data on different phases (Ringwood and Seabrook, 1963; Liu, 1977; Hattori et al. 2001;

587Nakatsuka et al. 2013). The dashed grey lines are the phase boundaries in GeO$_2$ (after Ono et al.

5862003). The dashed black lines are extrapolations of the data points and not an indication of the

587Clapeyron slopes.
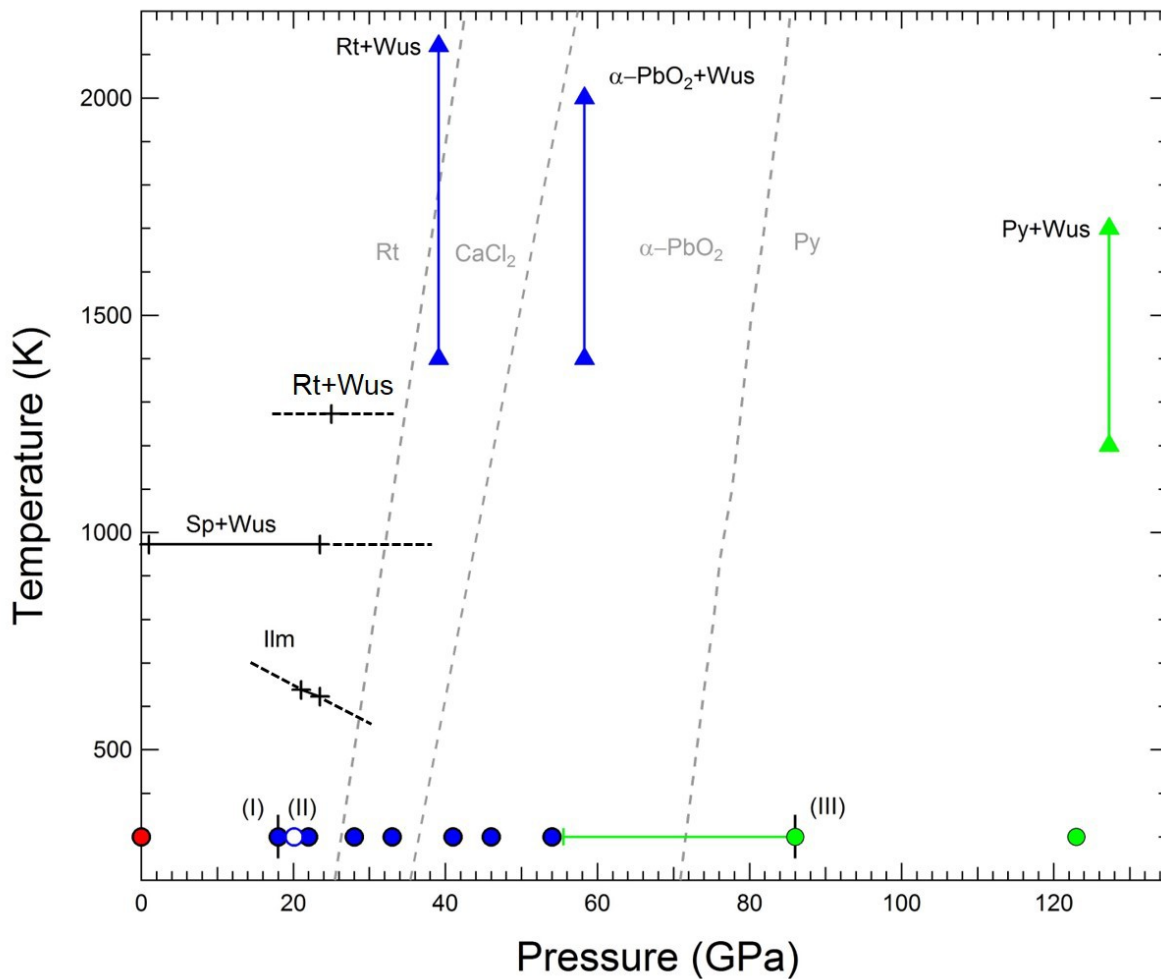
588

589

590Table I. Experimental conditions and observed phases.

591

Sample ID	Pressure medium	P/T condition (GPa/K)	Phases present
S1	Neon	39.1 / 2120	Rutile GeO_2 + FeO-B1
		33.9 / 300	$CaCl_2$ GeO_2 + FeO-B1 +FeO-rB1

S2	Neon	58.3 / 2000 K	α-PbO$_2$ GeO$_2$ + FeO-B1
S3	N/A	127.3 / 1700	Pyrite GeO$_2$ + FeO-B1

592

593 Table 2. Comparison of the observed *d*-spacings of $FeGeO_3$ at 41 GPa with those of perovskite at

594 40 GPa as reported by Hattori et al. (1999).

595

596

This Study (41 GPa) d_{obs} (Å)	Perovskite, Hattori et al., 1999 (40 GPa)		
	d_{obs} (Å)	d_{calc} (Å)	(*hkl*)
	3.52	3.533	110
	3.333	3.333	002
2.668			
2.587			
2.504			
2.422	2.444	2.530	020
2.365	-	2.467	200
2.038	-	2.424	112
2.011			
	1.765	1.766	220
	1.665	1.667	004
1.407	1.416	1.440	132

597

598

599

600

601

602

603

604

605

606

607

608Table 3. Calculated and observed d-spacings and their difference for rutile-type GeO_2 at 39.1

609GPa and 2120 K (GeO_2: a = 4.2462 (17) Å, c = 2.8122 (23) Å, and FeO-B1 (a = 4.1454 (11) Å).

610

611GeO_2 (rutile):

h	k	l	d_{obs} (Å)	d_{calc} (Å)	Δd (Å)
1	1	0	2.99873	3.00256	-0.00383
0	1	1	2.34516	2.34467	0.00049
0	2	0	2.12493	2.12313	0.0018
1	2	1	1.57346	1.57379	-0.00033

612

613

614FeO (B1):

h	k	l	d_{obs} (Å)	d_{calc} (Å)	Δd (Å)
1	1	1	2.39398	2.39333	0.00065
0	0	2	2.07284	2.07268	0.00015
0	2	2	1.46541	1.46561	-0.0002

615

616

617

618Table 4. Unit cell dimensions and atomic positions of GeO_2 and FeO obtained from Rietveld refinement. Numbers in parentheses

619denote the uncertainties in refinement. Z represents the number of formula units.

Pressure, Temperature	Phase	Space Group	Lattice Parameters (Å)	Site	Wyckoff Symbol	Fractional Coordinates	R_p/R_{wp}*
39.1 GPa, 2120 K	GeO_2 (Rutile)	$P4_2/mnm$ Z = 2	a = 4.2497 (2) c = 2.8192 (2)	Ge: O:	2(a) 4(f)	(0, 0, 0) (0.2874 (15), 0.2874 (15), 0)	0.0137/ 0.0202
	FeO (B1)	$Fm\bar{3}m$ Z = 4	a = 4.1431 (12)				
33.9 GPa, 300 K	GeO_2 (CaCl₂)	$Pnnm$ Z = 2	a = 4.2831 (5) b = 4.1669 (4) c = 2.7991 (3)	Ge: O:	2(a) 4(g)	(0, 0, 0) (0.3089 (19), 0.2846 (17), 0)	0.0097/ 0.0137
	FeO (rB1)	$R\bar{3}m$ Z = 2	a = 2.8242 (49) c = 7.4044 (94)				
	FeO (B1)	$Fm\bar{3}m$ Z = 4	a = 4.1071 (5)				
58.3 GPa, 2000 K	GeO_2 (α-PbO₂)	$Pbcn$ Z = 4	a = 4.1005 (10) b = 5.0997 (15) c = 4.5825 (8)	Ge: O:	4(c) 8(d)	(0, 0.1678 (7), 0.25) (0.2251 (28), 0.8744 (79), 0.4132 (46))	0.0077/ 0.0109
	FeO (B1)	$Fm\bar{3}m$ Z = 4	a = 4.0545 (6)				
127.3 GPa 1700 K	GeO_2 (Pyrite)	$Pa\bar{3}$ Z = 4	a = 4.3226 (2)	Ge: O:	4(a) 8(c)	(0, 0, 0) (0.3347 (7), 0.3347 (7), 0.3347 (7))	0.0067/ 0.0095
	FeO (B1)	$Fm\bar{3}$	a = 3.7896 (17)				

		m $Z = 4$					

620

621* $R_p = \sum w_i |y_i(obs) - y_i(calc)| / \sum y_i(obs)$; $R_\wp = \left\{ \sum w_i [y_i(obs) - y_i(calc)]^2 / w_i [y_i(obs)]^2 \right\}^{1/2}$; where w is the weight, $y_i(obs)$

622and $y_i(calc)$ are the observed and calculated intensities after background subtraction.